

Anisotropic Thermal Transport in Phase-Transition Layered 2D Alloys $\text{WSe}_{2(1-x)}\text{Te}_{2x}$

Xin Qian^{1#}, Puqing Jiang^{1#}, Peng Yu^{2#}, Xiaokun Gu³, Zheng Liu^{2*} and Ronggui Yang^{1*}

¹Department of Mechanical Engineering, University of Colorado, Boulder, CO 80309

²Center for Programmable Materials, School of Materials Science & Engineering, Nanyang Technological University, 639798, Singapore

³Institute of Engineering Thermophysics, Shanghai Jiao Tong University, Shanghai, 200240

*Email: Ronggui.Yang@Colorado.Edu

Z.Liu@NTU.edu.sg

These authors contribute equally to this work.

Abstract

Transition metal dichalcogenide (TMD) alloys have attracted great interests in recent years due to their tunable electronic properties, especially the semiconductor-metal phase transition, along with their potential applications in solid-state memories and thermoelectrics. However, the thermal conductivity of layered two-dimensional (2D) TMD alloys remains largely unexplored despite that it plays a critical role in the reliability and functionality of TMD-enabled devices. In this work, we study the temperature-dependent anisotropic thermal conductivity of the phase-transition 2D TMD alloys $\text{WSe}_{2(1-x)}\text{Te}_{2x}$ in both the in-plane direction (parallel to the basal planes) and the cross-plane direction (along the c -axis) using time-domain thermoreflectance measurements. In the $\text{WSe}_{2(1-x)}\text{Te}_{2x}$ alloys, the cross-plane thermal conductivity is observed to be dependent on the heating frequency (modulation frequency of the pump laser) due to the non-equilibrium transport between different phonon modes. Using a two-channel heat conduction model, we extracted the anisotropic thermal conductivity at the equilibrium limit. A clear discontinuity in both the cross-plane and the in-plane thermal conductivity is observed as x increases from 0.4 to 0.6 due to the phase transition from the 2H to Td phase in the layered 2D alloys. The temperature dependence of thermal

conductivity for the TMD alloys was found to become weaker compared with the pristine 2H WSe₂ and Td WTe₂ due to the atomic disorder. This work serves as an important starting point for exploring phonon transport in layered 2D alloys.

Transition metal dichalcogenides (TMDs) are a family of layered two-dimensional (2D) materials showing promising applications in electronics,¹⁻³ photonics,⁴⁻⁶ hydrogen evolution catalysts,⁷⁻⁹ and energy conversion and storage.¹⁰⁻¹² Alloys of layered 2D TMDs are of particular interest due to their tunable properties.¹³⁻¹⁴ For example, electronic bandgaps can be continuously changed in several TMD alloy systems including $\text{MoS}_{2(1-x)}\text{Se}_{2x}$,¹⁵⁻¹⁶ $\text{W}_x\text{Mo}_{1-x}\text{S}_2$ ¹⁷⁻¹⁸ and $\text{W}_x\text{Mo}_{1-x}\text{Se}_2$.¹⁹ With intrinsically large electronic power factor of TMDs,²⁰⁻²² alloying the layered TMDs could potentially lead to highly efficient thermoelectrics where the thermal conductivity can be effectively reduced due to the mass-disorder scattering.²³⁻²⁴ Along this line, Gu *et al.*²⁵ performed a first-principles study on the thermal conductivity of $\text{MoS}_{2(1-x)}\text{Se}_{2x}$ monolayers, and predicted an order-of-magnitude reduction in the thermal conductivity of these alloys as compared with those of the pristine MoS_2 and MoSe_2 . However, there yet exists any experimental work on anisotropic thermal transport in layered TMD alloys, especially as a function of alloy compositions.

Intrigued by the unique electronic structures²⁶⁻²⁸ and the abundant phase transition²⁹⁻³⁰ in MoTe_2 and WTe_2 , MoTe_2 or WTe_2 based TMD alloys have also attracted intensive research, especially on the manipulation of the physical properties through controlling the phase transitions. For example, the topological electronic states of $\text{W}_x\text{Mo}_{1-x}\text{Te}_2$ can be effectively manipulated by the alloys composition.³¹ The hysteresis of the cross-plane thermal conductivity during the 1T'-to-Td phase transition of $\text{W}_x\text{Mo}_{1-x}\text{Te}_2$ is also observed, and the phase change point can be tuned to room temperature,³² which makes it a promising material for phase change memory devices.³³ Depending on the composition, $\text{WSe}_{2(1-x)}\text{Te}_{2x}$ also exhibits a 2H-to-Td phase transition, which can be used for bandgap tuning.³⁴ Such phase transition in ternary TMD alloys could be potentially exploited for optimizing thermoelectric performances.³⁵ However, there exists no study on how such a phase transition would affect the thermal transport properties.

In this Letter, we study the composition-dependent and temperature dependent anisotropic thermal conductivity of the ternary alloy of layered 2D $\text{WSe}_{2(1-x)}\text{Te}_{2x}$ using an integrated experimental-theoretical approach with the time-domain thermoreflectance (TDTR) measurements. [Figure 1a-b](#) shows that atomic structure of the ternary TMD alloy $\text{WSe}_{2(1-x)}\text{Te}_{2x}$ can be in both 2H phase and Td phase. When the Se atom occupies the majority of the chalcogen sites, the TMD alloy shows a hexagonal 2H phase. A phase transition to the orthorhombic Td phase would happen when Te atom becomes the majority. We prepared single crystalline samples of the layered 2D TMD alloys for the measurement of composition dependent thermal conductivity. The composition fraction x of the $\text{WSe}_{2(1-x)}\text{Te}_{2x}$ crystals is varied from zero to one, including the pure WSe_2 ($x = 0$), $\text{WSe}_{1.8}\text{Te}_{0.2}$ ($x = 0.1$), $\text{WSe}_{1.6}\text{Te}_{0.4}$ ($x = 0.2$), $\text{WSe}_{1.2}\text{Te}_{0.8}$ ($x = 0.4$), $\text{WSe}_{0.8}\text{Te}_{1.2}$ ($x = 0.6$), $\text{WSe}_{0.4}\text{Te}_{1.6}$ ($x = 0.8$), and WTe_2 ($x = 1.0$). These samples are synthesized by chemical vapor transport in a one-step process and the details of synthesis are described in [Supporting Information S1](#). Typical structure of the 2H and Td alloy samples are shown in [Figure 1c](#) ($\text{WSe}_{1.2}\text{Te}_{0.8}$) and [Figure 1d](#) ($\text{WSe}_{0.4}\text{Te}_{1.6}$), respectively. In addition, x-ray diffraction (XRD) and energy dispersive x-ray (EDX) results show that the single crystals of $\text{WSe}_{1.2}\text{Te}_{0.8}$ ([Figure 1e](#)) and $\text{WSe}_{0.4}\text{Te}_{1.6}$ ([Figure 1f](#)) used in this work crystallize in 2H and 1Td structures, respectively, which are consistent with the nominal compositions (Inset, [Figure 1e-f](#)).³⁴

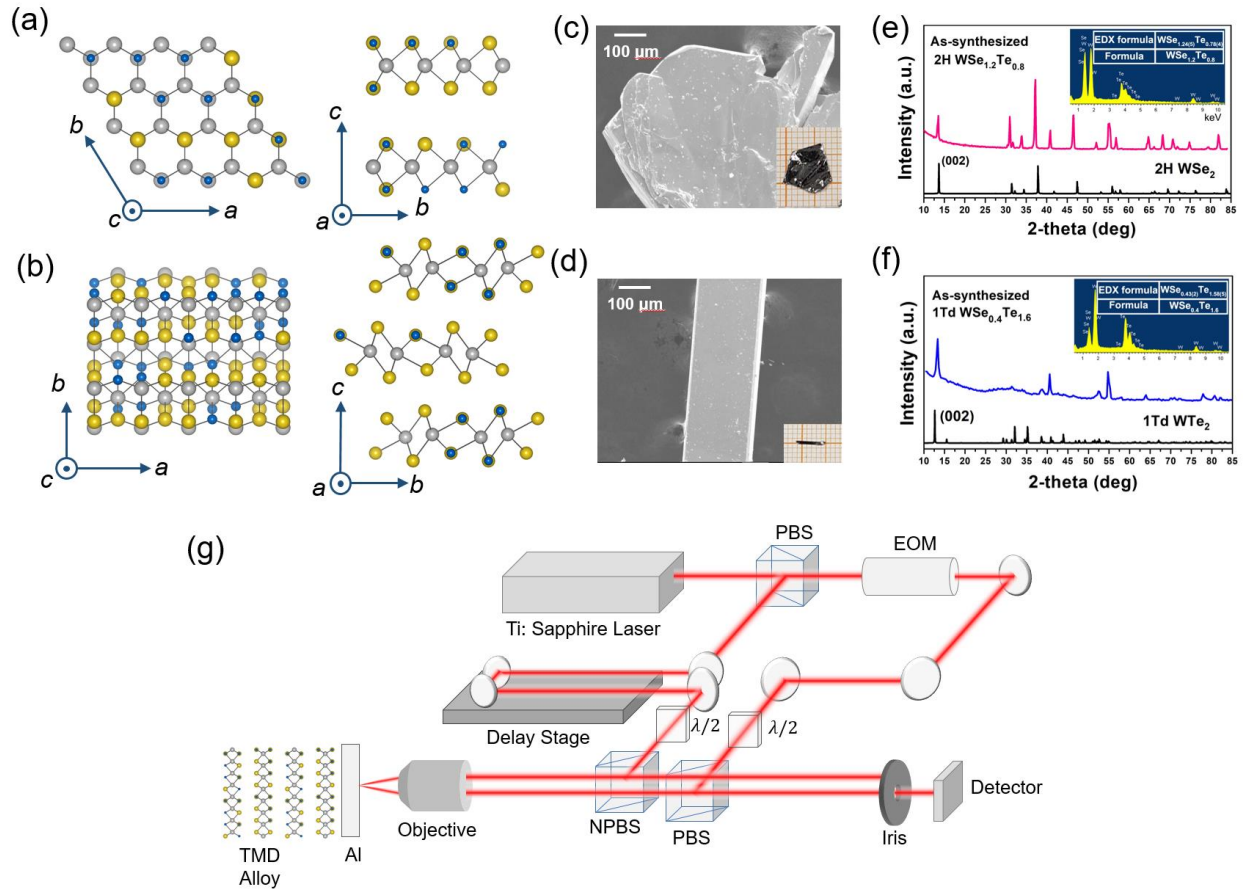


Figure 1. (a) Top view and side view of the structure of the layered 2D TMD alloy in 2H phase. The gray, blue and yellow spheres (not to scale) represent W, Se and Te atoms, respectively. (b) Top view and side view of the structure of the layered 2D TMD alloy in Td phase. (c-d) SEM and optical (inset) images of (c) 2H $\text{WSe}_{1.2}\text{Te}_{0.8}$ and (d) Td $\text{WSe}_{0.4}\text{Te}_{1.6}$. The scale bar of SEM images are 100 μm , and each grid in the optical image is 1mm-by-1mm. (e-f) XRD and EDX (inset) characterization of (e) 2H $\text{WSe}_{1.2}\text{Te}_{0.8}$ and (f) Td phase $\text{WSe}_{0.4}\text{Te}_{1.6}$. (g) Schematic of the TDTR system used for measuring the anisotropic thermal conductivity. Abbreviations are listed as follows: EOM, electric-optical modulator; PBS/NPBS, polarized/non-polarized beam splitter; $\lambda/2$, half wave plate.

We measure the anisotropic thermal conductivity of layered 2D TMD alloys using a femtosecond laser-based TDTR system as shown in Figure 1g. This system splits the femtosecond laser into a pump beam and a probe beam. The pump beam is modulated by an electric-optical modulator (EOM) at a typical frequency from 0.3 MHz to 10 MHz to create a periodic thermal

excitation on the surface of TMD alloy samples, where the surface of TMD alloy samples are deposited with an aluminum metal thin film (~ 75 nm). This Al transducer film absorbs the pump beam and its reflectance changes linearly with the surface temperature rise. The surface temperature change is monitored by detecting the reflected signal of the probe beam which is delayed to arrive at the sample surface by a translational delay stage. The transient surface temperature response is described by the ratio $-V_{in}/V_{out}$ between the in-phase signal V_{in} and the out-of-phase signal V_{out} , as shown in Figure 2a. The transient curve is fitted by solving a model for heat conduction in multi-layers using the nonlinear least squared regression to extract the thermal properties.³⁶⁻³⁸ Details of our TDTR system along with the data reduction method can be seen in our previous publications.³⁹⁻⁴⁰

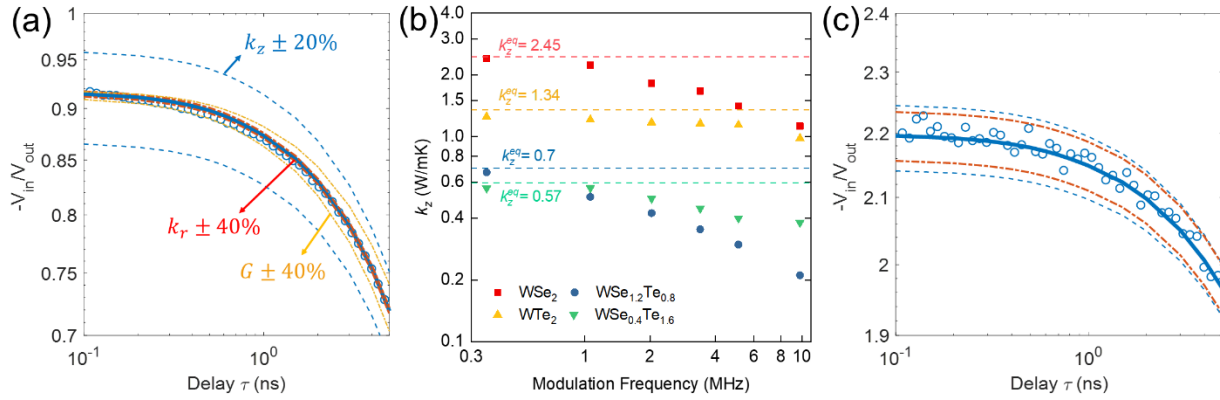


Figure 2. (a) Measured TDTR signal for $WSe_{1.2}Te_{0.8}$ using 76 nm Al transducer, a root-mean-square spot radius $w = 8.4 \mu\text{m}$ and a modulation frequency $f_0 = 2.16$ MHz. The TDTR signal is dominantly sensitive to k_z . The best-fit cross-plane thermal conductivity is $k_z = 0.42$ W/mK. (b) Frequency dependent k_z of WSe_2 , $WSe_{1.2}Te_{0.8}$, $WTe_{1.6}Se_{0.4}$ and WTe_2 . (c) Measuring in-plane thermal conductivity of $WTe_{1.2}Se_{0.8}$ sample using $w = 4.2 \mu\text{m}$. The best-fit $k_r = 10.1$ W/mK.

Since the TMD alloys are layered 2D crystals with drastically different in-plane bonding and interlayer bonding, the thermal conductivity should be strongly anisotropic along the in-plane and

cross-plane directions. In TDTR, we can separately determine the in-plane and cross-plane thermal conductivity by choosing appropriate operational parameters, i.e. the modulation frequency f_0 and the root-mean-squared laser spot radius w between the pump spot radius w_0 and probe spot radius w_1 , i.e., $w = \sqrt{w_0^2 + w_1^2}$.⁴⁰ When the laser spot radius w is much larger than the penetration depth $d_p = \sqrt{k_r/\pi C f_0}$ with k_r the in-plane thermal conductivity, C the volumetric heat capacity and f_0 the modulation frequency, the temperature field is quasi-one-dimensional in the cross-plane direction, and the TDTR is only sensitive to the cross-plane thermal conductivity k_z .⁴⁰ In [Figure 2a](#), we show an example of measuring k_z of $\text{WSe}_{1.2}\text{Te}_{0.8}$ with WTe_2 fraction $x = 0.4$ using a spot radius $w = 8.4 \mu\text{m}$. The signal $-V_{in}/V_{out}$ is sensitive to k_z only, especially when the probe delay time is shorter than 1 ns. This allows us to measure k_z independently of k_r and the interface conductance G with the Al transducer. Interestingly, we observed that the measured thermal conductivity k_z decreases as the modulation frequency increases ([Figure 2b](#)), if the conventional heat conduction model with one effective thermal conductivity value^{36, 38} for the data analysis. Such frequency-dependent k_z was also observed in other layered 2D crystals like pure TMDs³⁹ and in black phosphorus.⁴¹ Jiang and Qian *et al.* explained this as the non-equilibrium phonon transport between the low frequency and high frequency phonon modes.³⁹ In the cross-plane direction, the thermal conductivity is mainly contributed by the low frequency phonons with small heat capacity, while the high frequency phonons with large heat capacity have negligible thermal conductivity due to their “flat” phonon bandstructure.³⁹ Such a large mismatch between heat conductivity and heat capacity of different frequency bands of phonons tends to be in non-equilibrium. When the sample is subjected to periodic laser heating, the heat is accumulated in the high frequency phonons, resulting in their higher temperature than the low frequency phonons. To describe such non-equilibrium phonon transport, we use a two-channel heat conduction model⁴²

that separates the phonon heat carriers into the high frequency channel and the low frequency channel with their own temperatures, heat capacity and thermal conductivity. In this model, the cross-plane thermal conductivity at the equilibrium limit (k_z^{eq}) can be calculated by the summation of the thermal conductivity of both channels, indicated by the dash lines in [Figure 2b](#). (See [Supporting Information S3 to S5](#) for details of fitting, uncertainty analysis and division of phonon channels). After k_z^{eq} is determined, the laser spot is tightly focused to $w = 4.2 \mu\text{m}$, so that the TDTR signal becomes sensitive to both the cross-plane thermal conductivity k_z^{eq} and the in-plane thermal conductivity k_r . As shown in [Figure 2c](#), the in-plane thermal conductivity of $\text{WSe}_{1.2}\text{Te}_{0.8}$ is measured to $k_r = 10.1 \text{ W/mK}$ with a spot radius of $4.2 \mu\text{m}$ and a modulation frequency of 0.353 MHz .

Using a similar method as described above, we have measured the in-plane and cross-plane thermal conductivity of all TMD samples as summarized in [Figure 3a](#) and [Figure 3b](#), respectively. We compare the thermal conductivity of the pure WSe_2 and WTe_2 crystals with the results available in the literature. For WSe_2 , our measurements for both $k_r = 40 \text{ W/mK}$ and $k_z = 2.45 \text{ W/mK}$ are consistent with our previous work³⁹ and the first principles calculations by Lindroth *et al.*⁴³ However, the measured k_z is significantly higher than the TDTR measurements by Chiritescu *et al.*⁴⁴ and Murato *et al.*,⁴⁵ probably because they neglected non-equilibrium transport. For WTe_2 , our measurement for the in-plane thermal conductivity ($k_r = 13.5 \text{ W/mK}$) agrees well with the measurement by Zhou *et al.* ($k_r = 15 \text{ W/mK}$).⁴⁶ Interestingly, the k_r of WTe_2 measured by TDTR is even higher than the first principles calculation of lattice thermal conductivity. There are two possible reasons for such discrepancy. First of all, the electrons might have a notable contribution to the total thermal conductivity measured by the TDTR since WTe_2 is a semi-metal,⁴⁷ while it was completely neglected by the first principle calculations of lattice thermal conductivity.

The other possible reason is likely due to the computational error. WTe_2 has a rather complicated atomic structure. However, in the calculation by Liu *et al.*,⁴⁸ the authors used a relative small supercell ($2 \times 2 \times 1$ unit cells) for calculating the force constants to mitigate the large computation cost, which might lead to an underestimated thermal conductivity.⁴³ In the cross-plane direction, our measurement is $k_z = 1.34$ W/mK, which agrees well with both the first principles calculations⁴⁸ and the measurements by others.^{46, 49-50} For both the in-plane and the cross-plane direction, the thermal conductivity reduces as the composition fraction x or $(1-x)$ in $\text{WSe}_{2(1-x)}\text{Te}_{2x}$ approaches 0.5. The sharp change of thermal conductivity in both in-plane and cross-plane directions are observed as x increases from 0.4 to 0.6. This is due to the phase transition from the 2H to Td phase as x increases from 0.4 to 0.6. Since phase transition has also been used for enhancing thermoelectric figure of merit (ZT) for other calcogenides like SnSe ⁵¹, Cu_2Se ⁵² and so on, such a phase transition of 2H to Td could potentially result in a higher ZT factor due to the decreased thermal conductivity both along the in-plane direction and the cross-plane direction.

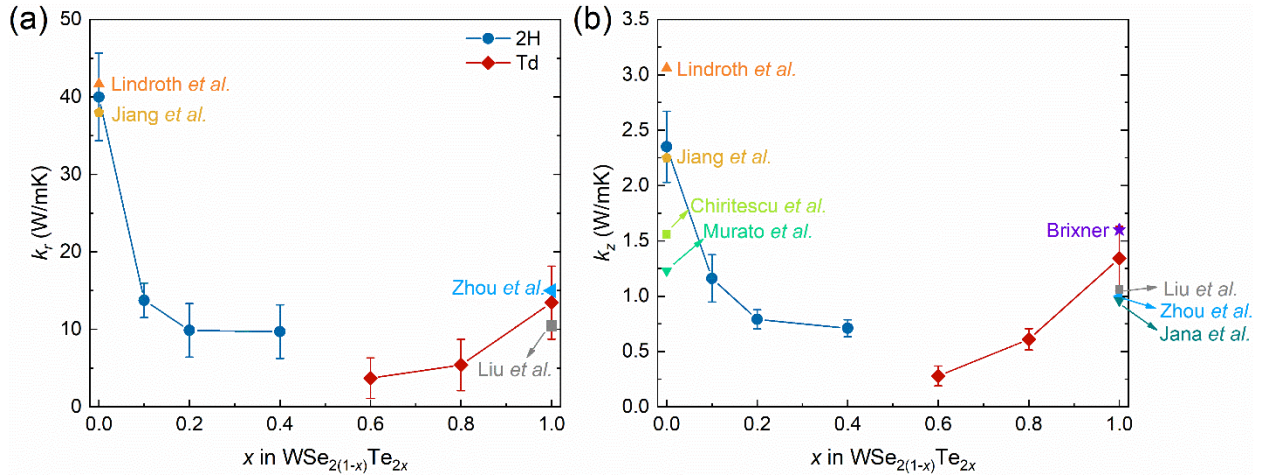


Figure 3. Composition dependent (a) In-plane thermal conductivity and (b) cross-plane thermal conductivity of $\text{WSe}_{2(1-x)}\text{Te}_{2x}$ measured by TDTR. The thermal conductivity of pristine WSe_2 ($x=0$) and WTe_2 ($x=1$) are compared with first-principles calculations by Lindroth *et al.*⁴³ and Liu *et al.*,⁴⁸ and measurement by Jiang *et al.*,³⁹ Chiritescu *et al.*,⁴⁴ Murato *et al.*,⁴⁵ Zhou *et al.*,⁴⁶ Brixner *et al.*⁴⁹ and Jana *et al.*⁵⁰

In [Figure 4](#), we show the temperature-dependent k_r and k_z of the 2H $\text{WSe}_{1.2}\text{Te}_{0.8}$ ($x=0.4$) and Td $\text{WSe}_{0.4}\text{Te}_{1.6}$ ($x=0.8$), in comparison with the pure 2H WSe_2 and Td WTe_2 , respectively. In the entire temperature range from 80 K to 300 K, both k_r and k_z of 2H $\text{WSe}_{1.2}\text{Te}_{0.8}$ are greatly reduced compared with the pure WSe_2 due to the alloy scattering, and a similar reduction is also observed in $\text{WSe}_{0.4}\text{Te}_{1.6}$ in the Td phase compared with WTe_2 . As shown in [Figure 4a](#) and [Figure 4c](#), the $k_r(T)$ curve flattens below 150 K for both 2H $\text{WSe}_{1.2}\text{Te}_{0.8}$ and Td $\text{WSe}_{0.4}\text{Te}_{1.6}$, while k_r kept increasing with the temperature for the pristine WSe_2 and WTe_2 . Since the alloy scattering due to mass disorder is temperature independent,⁵³ it becomes more dominant at lower temperature when the intrinsic three phonon scattering is much weaker at cryogenic temperature, contributing to the weaker temperature dependence of k_r below 150 K. It is interesting to note that the $k_z(T)$ curve of $\text{WSe}_{0.4}\text{Te}_{1.6}$ is much flatter than the $k_z(T)$ curve WTe_2 , as shown [Figure 4d](#). Since $\text{WSe}_{0.4}\text{Te}_{1.6}$ has randomly distributed Se defects, the distribution pattern of the defects is expected to be very different in each monolayer, which breaks the periodicity in the cross-plane direction. As a result of such atomic disorder, the vibration modes are greatly localized in the cross-plane direction, resulting in the much lower k_z value and a much flatter $k_z(T)$ curve than the pristine TMD crystal. For the same reason, the $k_z(T)$ curve of $\text{WSe}_{1.2}\text{Te}_{0.8}$ showed a similar shape compared to $\text{WSe}_{0.4}\text{Te}_{1.6}$, as shown in [Figure 4b](#) and [Figure 4d](#). However, the temperature dependence of k_z of WSe_2 is very different from WTe_2 . Instead of increasing with decreasing temperature, the $k_z(T)$ curve of WSe_2 showed a peak near 150 K. Suggested by the Lindroth et al.⁴³ and Jiang et al.,³⁹ there could exist stacking faults that induce boundary scattering on the length scale of ~ 150 nm,⁴³ resulting in such a peak in the $k_z(T)$ curve and much lower k_z compared with first principles calculations. However, such peak in the $k_z(T)$ curve is absent in the WTe_2 . Such different behavior of temperature dependent k_z can be explained by the different distribution of phonon mean free

paths (MFPs) in WTe₂ and WSe₂. As suggested by the first principles calculations, half of k_z of WTe₂ is contributed by phonons with MFPs between 200 nm to 1 μm ,⁴⁸ but 50% of k_z of WSe₂ is contributed by phonons with MFPs above 1 μm .⁴³ Due to the much longer MFPs in WSe₂ than WTe₂, the stacking faults are expected to have a much more pronounced effect on k_z in WSe₂ than WTe₂.

In summary, we applied the ultrafast laser based TDTR technique to study the temperature-dependent anisotropic thermal transport of layered 2D TMD alloys WSe_{2(1-x)}Te_{2x}. We observed that the cross-plane thermal conductivity depends on the modulation frequency of the TDTR pump beam, due to the non-equilibrium transport between different phonon modes in the cross-plane direction. A two-channel heat conduction model is used to extract the cross-plane thermal conductivity at the thermal equilibrium limit. The in-plane thermal conductivity is then determined using a tightly focused laser spot with radius of 4.2 μm . Both the in-plane and cross-plane thermal conductivity is reduced at higher alloy mixing level as the composition fraction x or $(1-x)$ in WSe_{2(1-x)}Te_{2x} approaches 0.5. A clear discontinuity in both the cross-plane and the in-plane thermal conductivity is observed as x increases from 0.4 to 0.6 due to the phase transition from the 2H to Td phase in the layered 2D alloys. We also found that the temperature dependence of thermal conductivity for the TMD alloys becomes weaker compared with the pristine 2H WSe₂ and Td WTe₂ due to the atomic disorder. This work serves as an important starting point for exploring phonon transport physics in layered 2D alloys.

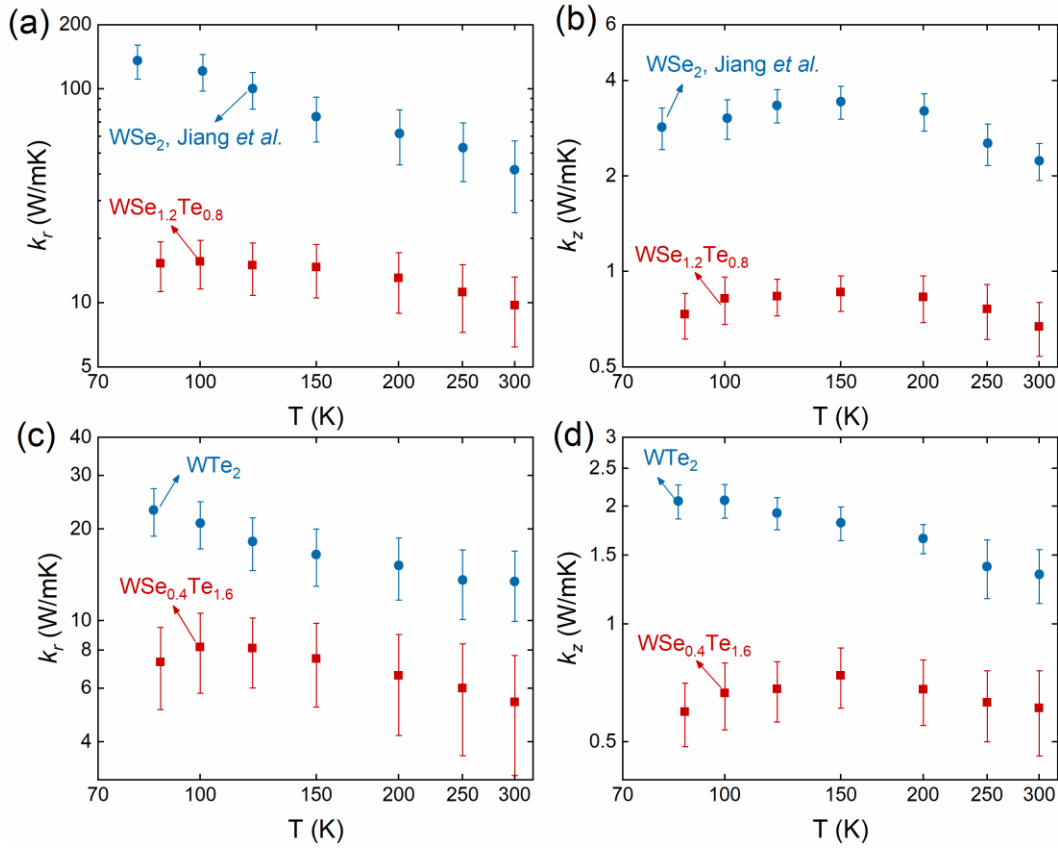


Figure 4. Temperature dependent (a) in-plane thermal conductivity and (b) cross-plane thermal conductivity of 2H WSe₂ and WSe_{1.2}Te_{0.8} ($x=0.4$), and temperature dependent (c) in-plane thermal conductivity and (d) cross-plane thermal conductivity of WTe₂ and WSe_{0.4}Te_{1.6} ($x=0.8$).

Acknowledgment: This work is supported by NSF (Grant No. 1512776). X. Q. acknowledges the helpful discussions with Jian Zhou and Gang Liu at Nanjing University. This work is also supported by the National Research Foundation Singapore under NRF Award No. NRF-RF2013-08.

References:

1. Manzeli, S.; Ovchinnikov, D.; Pasquier, D.; Yazyev, O. V.; Kis, A., 2d Transition Metal Dichalcogenides. *Nature Reviews Materials* **2017**, *2*, 17033.
2. Radisavljevic, B.; Radenovic, A.; Brivio, J.; Giacometti, V.; Kis, A., Single-Layer Mos2 Transistors. *Nature nanotechnology* **2011**, *6*, 147-50.
3. Cho, M. S.; Qu, D.; Lee, D.; Xiaochi Liu; Watanabe, K.; Taniguchi, T.; Yoo, W. J., Lateral Mos2 PN Junction Formed by Chemical Doping for Use in Highperformance Optoelectronics. *ACS Nano* **2014**, *8*, 9332-9340.
4. Lopez-Sanchez, O.; Lembke, D.; Kayci, M.; Radenovic, A.; Kis, A., Ultrasensitive Photodetectors Based on Monolayer Mos2. *Nature nanotechnology* **2013**, *8*, 497-501.
5. Mak, K. F.; He, K.; Shan, J.; Heinz, T. F., Control of Valley Polarization in Monolayer Mos2 by Optical Helicity. *Nature nanotechnology* **2012**, *7*, 494-8.
6. Yin, X.; Ye, Z.; Chenet, D. A.; Ye, Y.; O'Brien, K.; Hone, J. C.; Zhang, X., Edge Nonlinear Optics on a Mos2 Atomic Monolayer. *Science* **2014**, *344*, 488-490.
7. Chhowalla, M.; Shin, H. S.; Eda, G.; Li, L. J.; Loh, K. P.; Zhang, H., The Chemistry of Two-Dimensional Layered Transition Metal Dichalcogenide Nanosheets. *Nature chemistry* **2013**, *5*, 263-75.
8. Karunadasa, H. I.; Montalvo, E.; Sun, Y.; Majda, M.; Long, J. R.; Chang, C. J., A Molecular Mos2 Edge Site Mimic for Catalytic Hydrogen Generation. *Science* **2012**, *335*, 698-702.
9. Jaramillo, T. F.; Jørgensen, K. P.; Bonde, J.; Nielson, J. H.; Horch, S.; Chorkendorff, I., Identification of Active Edge Sites for Electrochemical H2 Evolution from Mos2 Nanocatalysts. *Science* **2007**, *317*, 100-102.
10. Wan, C.; Gu, X.; Dang, F.; Itoh, T.; Wang, Y.; Sasaki, H.; Kondo, M.; Koga, K.; Yabuki, K.; Snyder, G. J.; Yang, R.; Koumoto, K., Flexible N-Type Thermoelectric Materials by Organic Intercalation of Layered Transition Metal Dichalcogenide Tis2. *Nat. Mater.* **2015**, *14*, 622-7.
11. Wang, H.; Lu, Z.; Kong, D.; Sun, J.; Hymel, T. M.; Cui, Y., Electrochemical Tuning of Mos2 Nanoparticles on Three-Dimensional Substrate for Efficient Hydrogen Evolution. *ACS Nano* **2014**, *8*, 4940-4947.
12. Seh, Z. W.; Yu, J. H.; Li, W.; Hsu, P. C.; Wang, H.; Sun, Y.; Yao, H.; Zhang, Q.; Cui, Y., Two-Dimensional Layered Transition Metal Disulphides for Effective Encapsulation of High-Capacity Lithium Sulphide Cathodes. *Nature communications* **2014**, *5*, 5017.
13. Xie, L. M., Two-Dimensional Transition Metal Dichalcogenide Alloys: Preparation, Characterization and Applications. *Nanoscale* **2015**, *7*, 18392-401.
14. Castellanos-Gomez, A., Why All the Fuss About 2d Semiconductors? *Nature Photonics* **2016**, *10*, 202-204.
15. Feng, Q.; Zhu, Y.; Hong, J.; Zhang, M.; Duan, W.; Mao, N.; Wu, J.; Xu, H.; Dong, F.; Lin, F.; Jin, C.; Wang, C.; Zhang, J.; Xie, L., Growth of Large-Area 2d Mos2((1-X) Se2)X Semiconductor Alloys. *Adv. Mater.* **2014**, *26*, 2648-53, 2613.
16. Li, H.; Duan, X.; Wu, X.; Zhuang, X.; Zhou, H.; Zhang, Q.; Zhu, X.; Hu, W.; Ren, P.; Guo, P.; Ma, L.; Fan, X.; Wang, X.; Xu, J.; Pan, A.; Duan, X., Growth of Alloy Mos(2x)Se2(1-x) Nanosheets with Fully Tunable Chemical Compositions and Optical Properties. *J. Am. Chem. Soc.* **2014**, *136*, 3756-9.
17. Chen, Y.; Xi, J.; Dumcenco, D. O.; Liu, Z.; Suenaa, K.; Wang, D.; Shuai, Z.; Huang, Y.-S.; Xie, L., Tunable Band Gap Photoluminescence from Atomically Thin Transition-Metal Dichalcogenide Alloys. *ACS Nano* **2013**, *7*, 4610-4616.
18. Dumcenco, D. O.; Kobayashi, H.; Liu, Z.; Huang, Y. S.; Suenaga, K., Visualization and Quantification of Transition Metal Atomic Mixing in Mo1-XwxS2 Single Layers. *Nature communications* **2013**, *4*, 1351.

19. Zhang, M.; Wu, J.; Zhu, Y.; Dumcenco, D. O.; Hong, J.; Mao, N.; Deng, S.; Chen, Y.; Yang, Y.; Jin, C.; Chaki, S. H.; Huang, Y.-S.; Zhang, J.; Xie, L., Two-Dimensional Molybdenum Tungsten Diselenide Alloys: Photoluminescence, Raman Scattering, and Electrical Transport. *ACS Nano* **2014**, *8*, 7130-7137.
20. Kayyalha, M.; Maassen, J.; Lundstrom, M.; Shi, L.; Chen, Y. P., Gate-Tunable and Thickness-Dependent Electronic and Thermoelectric Transport in Few-Layer Mos₂. *J. Appl. Phys.* **2016**, *120*, 134305.
21. Hippalgaonkar, K.; Wang, Y.; Ye, Y.; Qiu, D. Y.; Zhu, H.; Wang, Y.; Moore, J.; Louie, S. G.; Zhang, X., High Thermoelectric Power Factor in Two-Dimensional Crystals Ofmos₂. *Phys. Rev. B* **2017**, *95*.
22. Yoshida, M.; Iizuka, T.; Saito, Y.; Onga, M.; Suzuki, R.; Zhang, Y.; Iwasa, Y.; Shimizu, S., Gate-Optimized Thermoelectric Power Factor in Ultrathin Wse₂ Single Crystals. *Nano Lett* **2016**, *16*, 2061-5.
23. Klemens, P. G., The Scattering of Low-Frequency Lattice Waves by Static Imperfections. *Proc. Phys. Soc., Section A* **1955**, *68*, 1113.
24. Tian, Z.; Garg, J.; Esfarjani, K.; Shiga, T.; Shiomi, J.; Chen, G., Phonon Conduction in Pbse, Pbte, and Pbte_{1-x}sex from First-Principles Calculations. *Phys. Rev. B* **2012**, *85*.
25. Gu, X.; Yang, R., Phonon Transport in Single-Layermo_{1-x}wxs₂alloy Embedded Withws₂nanodomains. *Phys. Rev. B* **2016**, *94*.
26. Soluyanov, A. A.; Gresch, D.; Wang, Z.; Wu, Q.; Troyer, M.; Dai, X.; Bernevig, B. A., Type-II Weyl Semimetals. *Nature* **2015**, *527*, 495-8.
27. Jiang, J.; Liu, Z. K.; Sun, Y.; Yang, H. F.; Rajamathi, C. R.; Qi, Y. P.; Yang, L. X.; Chen, C.; Peng, H.; Hwang, C. C.; Sun, S. Z.; Mo, S. K.; Vobornik, I.; Fujii, J.; Parkin, S. S.; Felser, C.; Yan, B. H.; Chen, Y. L., Signature of Type-II Weyl Semimetal Phase in Mote₂. *Nature communications* **2017**, *8*, 13973.
28. Feng, B.; Chan, Y.-H.; Feng, Y.; Liu, R.-Y.; Chou, M.-Y.; Kuroda, K.; Yaji, K.; Harasawa, A.; Moras, P.; Barinov, A.; Malaeb, W.; Bareille, C.; Kondo, T.; Shin, S.; Komori, F.; Chiang, T.-C.; Shi, Y.; Matsuda, I., Spin Texture in Type-II Weyl Semimetal Wte₂. *Phys. Rev. B* **2016**, *94*.
29. Wang, Y.; Xiao, J.; Zhu, H.; Li, Y.; Alsaied, Y.; Fong, K. Y.; Zhou, Y.; Wang, S.; Shi, W.; Wang, Y.; Zettl, A.; Reed, E. J.; Zhang, X., Structural Phase Transition in Monolayer Mote₂ Driven by Electrostatic Doping. *Nature* **2017**.
30. Duerloo, K. A.; Li, Y.; Reed, E. J., Structural Phase Transitions in Two-Dimensional Mo- and W-Dichalcogenide Monolayers. *Nature communications* **2014**, *5*, 4214.
31. Belopolski, I.; Xu, S.-Y.; Ishida, Y.; Pan, X.; Yu, P.; Sanchez, D. S.; Zheng, H.; Neupane, M.; Alidoust, N.; Chang, G.; Chang, T.-R.; Wu, Y.; Bian, G.; Huang, S.-M.; Lee, C.-C.; Mou, D.; Huang, L.; Song, Y.; Wang, B.; Wang, G.; Yeh, Y.-W.; Yao, N.; Rault, J. E.; Le Fèvre, P.; Bertran, F.; Jeng, H.-T.; Kondo, T.; Kaminski, A.; Lin, H.; Liu, Z.; Song, F.; Shin, S.; Hasan, M. Z., Fermi Arc Electronic Structure and Chern Numbers in the Type-II Weyl Semimetal Candidatemoxw_{1-x}te₂. *Phys. Rev. B* **2016**, *94*.
32. Yan, X.-J.; Lv, Y.-Y.; Li, L.; Li, X.; Yao, S.-H.; Chen, Y.-B.; Liu, X.-P.; Lu, H.; Lu, M.-H.; Chen, Y.-F., Composition Dependent Phase Transition and Its Induced Hysteretic Effect in the Thermal Conductivity of Wxmo_{1-x}te₂. *Appl. Phys. Lett.* **2017**, *110*, 211904.
33. Duerloo, K. A.; Reed, E. J., Structural Phase Transitions by Design in Monolayer Alloys. *ACS Nano* **2016**, *10*, 289-97.
34. Yu, P.; Lin, J.; Sun, L.; Le, Q. L.; Yu, X.; Gao, G.; Hsu, C. H.; Wu, D.; Chang, T. R.; Zeng, Q.; Liu, F.; Wang, Q. J.; Jeng, H. T.; Lin, H.; Trampert, A.; Shen, Z.; Suenaga, K.; Liu, Z., Metal-Semiconductor Phase-Transition in Wse₂(1-x)Te_{2x} Monolayer. *Adv. Mater.* **2017**, *29*.
35. Zheng, Z.; Su, X.; Deng, R.; Stoumpos, C. C.; Xie, H.; Liu, W.; Yan, Y.; Hao, S.; Uher, C.; Wolverton, C.; Kanatzidis, M. G.; Tang, X., Rhombohedral to Cubic Conversion of GeTe Via MnTe Alloying Leads to Ultralow Thermal Conductivity, Electronic Band Convergence and High Thermoelectric Performance. *J. Am. Chem. Soc.* **2018**, *Just Accepted Manuscript*, DOI: 10.1021/jacs.7b13611.

36. Cahill, D. G., Analysis of Heat Flow in Layered Structures for Time-Domain Thermoreflectance. *Rev. Sci. Instrum.* **2004**, *75*, 5119-5122.
37. Liu, J.; Zhu, J.; Tian, M.; Gu, X.; Schmidt, A. J.; Yang, R., Simultaneous Measurement of Thermal Conductivity and Heat Capacity of Bulk and Thin Film Materials Using Frequency-Dependent Transient Thermoreflectance Method. *Rev. Sci. Instrum.* **2013**, *84*, 034902.
38. Schmidt, A. J., Pump-Probe Thermoreflectance. *Annual Review of Heat Transfer* **2013**, *16*, 159.
39. Jiang, P.; Qian, X.; Gu, X.; Yang, R., Probing Anisotropic Thermal Conductivity of Transition Metal Dichalcogenides Mx_2 ($M = Mo, W$ and $X = S, Se$) Using Time-Domain Thermoreflectance. *Adv. Mater.* **2017**, *29*, 1701068.
40. Jiang, P.; Qian, X.; Yang, R., Time-Domain Thermoreflectance (Tdtr) Measurements of Anisotropic Thermal Conductivity Using a Variable Spot Size Approach. *Rev. Sci. Instrum.* **2017**, *88*, 074901.
41. Sun, B.; Gu, X.; Zeng, Q.; Huang, X.; Yan, Y.; Liu, Z.; Yang, R.; Koh, Y. K., Temperature Dependence of Anisotropic Thermal-Conductivity Tensor of Bulk Black Phosphorus. *Adv. Mater.* **2017**, *29*, 1603297.
42. Wilson, R. B.; Feser, J. P.; Hohensee, G. T.; Cahill, D. G., Two-Channel Model for Nonequilibrium Thermal Transport in Pump-Probe Experiments. *Phys. Rev. B* **2013**, *88*, 144305.
43. Lindroth, D. O.; Erhart, P., Thermal Transport in Van Der Waals Solids from First-Principles Calculations. *Phys. Rev. B* **2016**, *94*, 115205.
44. Chiritescu, C.; Cahill, D. G.; Nguyen, N.; Johnson, D.; Bodapati, A.; Keblinski, P.; Zschack, P., Ultralow Thermal Conductivity in Disordered, Layered WSe_2 Crystals. *Science* **2007**, *315*, 351-353.
45. Muratore, C.; Varshney, V.; Gengler, J. J.; Hu, J. J.; Bultman, J. E.; Smith, T. M.; Shamberger, P. J.; Qiu, B.; Ruan, X.; Roy, A. K.; Voevodin, A. A., Cross-Plane Thermal Properties of Transition Metal Dichalcogenides. *Appl. Phys. Lett.* **2013**, *102*, 081604.
46. Zhou, Y.; Jang, H.; Woods, J. M.; Xie, Y.; Kumaravadivel, P.; Pan, G. A.; Liu, J.; Liu, Y.; Cahill, D. G.; Cha, J. J., Direct Synthesis of Large-Scale WTe_2 Thin Films with Low Thermal Conductivity. *Adv. Funct. Mater.* **2017**, *27*, 1605928.
47. Mleczko, M. J.; Xu, R. L.; Okabe, K.; Kuo, H. H.; Fisher, I. R.; Wong, H. S.; Nishi, Y.; Pop, E., High Current Density and Low Thermal Conductivity of Atomically Thin Semimetallic WTe_2 . *ACS Nano* **2016**, *10*, 7507-7514.
48. Liu, G.; Sun, H. Y.; Zhou, J.; Li, Q. F.; Wan, X.-G., First-Principles Study of Lattice Thermal Conductivity of $Td-WTe_2$. *New Journal of Physics* **2016**, *18*, 033017.
49. Brixner, L. H., Preparation and Properties of the Single Crystalline Ab_2 -Type Selenides and Tellurides of Niobium, Tantalum, Molybdenum and Tungsten. *J. Inorg. Nucl. Chem.* **1962**, *24*, 257-263.
50. Jana, M. K.; Singh, A.; Late, D. J.; Rajamathi, C. R.; Biswas, K.; Felser, C.; Waghmare, U. V.; Rao, C. N., A Combined Experimental and Theoretical Study of the Structural, Electronic and Vibrational Properties of Bulk and Few-Layer $Td-WTe_2$. *Journal of physics. Condensed matter : an Institute of Physics journal* **2015**, *27*, 285401.
51. Zhao, L. D.; Lo, S. H.; Zhang, Y.; Sun, H.; Tan, G.; Uher, C.; Wolverton, C.; Dravid, V. P.; Kanatzidis, M. G., Ultralow Thermal Conductivity and High Thermoelectric Figure of Merit in $SnSe$ Crystals. *Nature* **2014**, *508*, 373-7.
52. Brown, D. R.; Day, T.; Borup, K. A.; Christensen, S.; Iversen, B. B.; Snyder, G. J., Phase Transition Enhanced Thermoelectric Figure-of-Merit in Copper Chalcogenides. *APL Materials* **2013**, *1*, 052107.
53. Tamura, S.-i., Isotope Scattering of Dispersive Phonons in Ge. *Phys. Rev. B* **1983**, *27*, 858-866.

Supporting Information

Anisotropic Thermal Transport in Phase-Transition Layered 2D Alloys $\text{WSe}_{2(1-x)}\text{Te}_{2x}$

Xin Qian^{1#}, Puqing Jiang^{1#}, Peng Yu^{2#}, Xiaokun Gu³, Zheng Liu^{2*} and Ronggui Yang^{1*}

¹Department of Mechanical Engineering, University of Colorado, Boulder, CO 80309

²Center for Programmable Materials, School of Materials Science & Engineering, Nanyang Technological University, 649798, Singapore

³Institute of Engineering Thermophysics, Shanghai Jiao Tong University, Shanghai, 200240

*Email: Ronggui.Yang@Colorado.Edu

Table of Contents

S1. Preparation of TMD alloy samples

S2. Non-equilibrium phonon transport and the two-channel heat conduction model

S3. Data reduction of TDTR measurement using the two-channel model

S4. Uncertainty analysis

S5. Heat capacity of TMD alloys using the first principles calculations

Supporting Information

S1. Preparation of TMD alloy samples

Large, well-formed, single crystals of $WSe_{2(1-x)}Te_{2x}$ ($x = 0-1$) alloys were grown by chemical vapor transport (CVT) method with iodine (I) as the transporting gas. Stoichiometric amounts of tungsten (W) powder (99.9%, Sigma-Aldrich), selenium (Se) powder (99.95%, Sigma-Aldrich) and tellurium (Te) powder (99.95%, Sigma-Aldrich) with a total weight of 300 mg, plus an extra 40 mg of I as the transporting gas were sealed in an evacuated 20 cm long quartz tube under the vacuum at 10^{-6} Torr. The quartz tube was placed in a three-zone furnace. Firstly, the reaction zone was maintained at 850 °C for 30 h with the growth zone at 900 °C in order to prevent the transport of the product and a complete reaction; then the reaction zone was heated to 1010 °C and held for 7 days with the growth zone at 900 °C. Finally, the furnace was naturally cooled down to the room temperature and the single crystals were collected in the growth zone. Residuals were cleaned using acetone before measurement.

After preparing the TMD alloys, we collected the powder XRD patterns using a Rigaku DMAX 2500 diffractometer with monochromatized Cu-K α radiation at room temperature in the 2θ range of 5–50° with a scan step width of 0.05°. SEM and semi-quantitative microprobe analyses on $WSe_{2(1-x)}Te_{2x}$ ($x = 0-1$) alloys were performed with the aid of a field emission scanning electron microscope (FESEM, JSM-5410) equipped with an energy dispersive X-ray spectroscope (EDX, Oxford INCA).

S2. Non-equilibrium phonon transport and the two-channel heat conduction model

The frequency dependent k_z can be attributed to the non-equilibrium transport between the high frequency and low frequency phonons. In layered materials like TMDs, black phosphorus and TMD alloys, low frequency phonons contribute to the majority of the k_z , but only a small amount of the heat capacity. In contrast, the high frequency phonons have small contribution to the k_z due to their small group velocity, but contribute to the majority of the heat capacity of the material. In TMD materials, the thermal conductivity contributed by high frequency phonons is further suppressed because of the alloy scattering. Such a mismatch of the heat capacity and thermal conductivity between different phonon groups would result in a temperature difference when the sample is periodically heated by the laser. The heating would accumulate within the high frequency phonons because they dissipate much slower than the low frequency phonons with long mean free paths. To capture the non-equilibrium transport between different phonon groups within the TMD alloys, we use the two-channel heat conduction model as previously used to explain the thermal transport in TMD crystals and black phosphorus.¹⁻² This model assumes that the heat carriers can be divided into two groups, and each group satisfies the Fourier's heat conduction equation while g is the coupling strength between the two channels:

$$\begin{aligned} C_1 \frac{\partial T_1}{\partial t} &= \frac{k_{r1}}{r} \frac{\partial}{\partial r} \left(r \frac{\partial T_1}{\partial r} \right) + k_{z1} \frac{\partial^2 T_1}{\partial z^2} + g(T_2 - T_1) \\ C_2 \frac{\partial T_2}{\partial t} &= \frac{k_{r2}}{r} \frac{\partial}{\partial r} \left(r \frac{\partial T_2}{\partial r} \right) + k_{z2} \frac{\partial^2 T_2}{\partial z^2} + g(T_1 - T_2) \end{aligned} \quad (1)$$

Supporting Information

Here T_i , C_i , k_{ri} , k_{zi} are the temperature, the heat capacity, the in-plane thermal conductivity and the cross-plane thermal conductivity of i -th channel ($i = 1,2$), respectively. As shown in Figure S1, channel 1 in the Al transducer represents the electrons, and channel 2 in Al transducer represents the phonons. In the TMD alloys which is modeled as a substrate, channel 1 represents the low-frequency phonons and channel 2 represents high frequency phonons. Since there are two channels on each side of the Al/TMD alloys interface, the energy transport across the interface is described by a 2-by-2 matrix $[G_{ij}]$, with the elements G_{ij} meaning the conductance between channel i in Al and channel j in the TMD alloy. A detailed solution of the two-channel model can be found in ref. [1] and [2]. The division of phonon channels for TMD alloys are shown in Section S6.

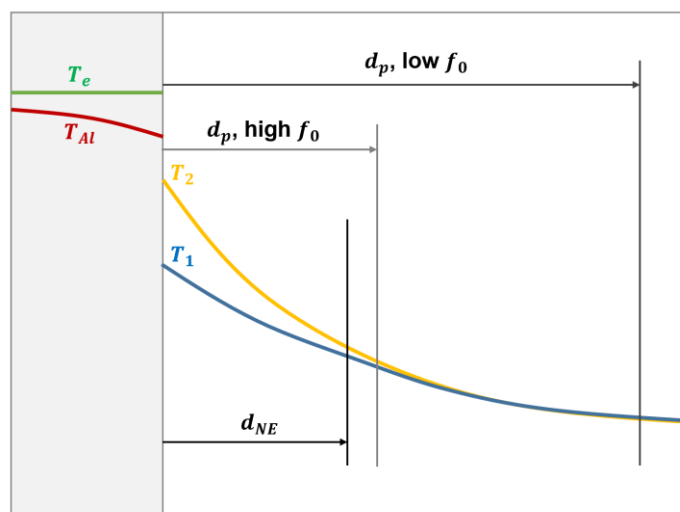


Figure S1. Schematic of the two-channel model for the non-equilibrium phonon transport.

Figure S1 illustrates that the neglect of non-equilibrium transport between high frequency and low frequency phonons in the TMD alloy substrate would result in frequency dependent k_z . The temperature difference between the two phonon channels is not negligible within a length scale $d_{NE} = \left(\frac{g}{k_{z1}} + \frac{g}{k_{z2}} \right)^{-1/2}$. The frequency dependence of the thermal conductivity k_z is caused by the neglect of such non-equilibrium transport when the conventional one-channel heat conduction model is used for data reduction. In the one-channel model, the length scale of temperature field in the sample is characterized by the penetration depth $d_p = \sqrt{k_z / \pi C f_0}$ with C the heat capacity and f_0 the modulation frequency, and TDTR measures the thermal property within the length scale of d_p . At high modulation frequency f_0 , d_p is comparable to d_{NE} and the non-equilibrium transport is not negligible. As a result, R_{NE} is grouped in to k_z when the one-channel model is used for data reduction, which would result in an underestimated k_z . When the f_0 is low, d_p is larger than d_{NE} , and the non-equilibrium resistance has less effect on k_z , thus k_z increases when f_0 decreases. For example, the non-equilibrium length of $\text{WSe}_{1.2}\text{Te}_{0.8}$ is estimated as $d_{NE} \approx 90$ nm, estimated from the parameters in Table S1. At high modulation frequency $f_0 = 9.8$ MHz, the

Supporting Information

penetration depth $d_p \approx 110$ nm, which is comparable to d_{NE} . When $f_0 = 0.353$ MHz, $d_p \approx 600$ nm, and the non-equilibrium transport has less effect on k_z .

S3. Data reduction of TDTR measurement using the two-channel model

For the transducer layer, the electronic thermal conductivity of Al is estimated to be 150 W/mK by using a four-point probe for electrical conductivity measurement, which is used as the value of k_{r1} and k_{z1} . The phononic thermal conductivity $k_{r2} = k_{z2} \approx 6$ W/mK, is estimated from first-principles calculations.³ The electron phonon coupling strength in Al transducer is taken as $g = 24.5 \times 10^{16}$ W/m³K.⁴ Since interfacial transport through the electron-phonon channel across the interface is usually negligible,¹ we apply adiabatic boundary condition for the electron channel in the Al transducer, so that $G_{11} = G_{12} = 0$.

The remaining unknown parameters of the TMD layers $\mathbf{U} = [k_{r1}, k_{r2}, k_{z1}, k_{z2}, G_{21}, G_{22}, g]^T$ need to be determined by matching the TDTR experimental signals. We conduct the sensitivity analysis so that in-plane properties k_{r1}, k_{r2} and the cross-plane properties can be measured separately. The sensitivity of the signal with respect to the parameter p is defined as:

$$S_p = \frac{\partial \ln \left(-\frac{V_{in}}{V_{out}} \right)}{\partial \ln p} \quad (2)$$

where $-\frac{V_{in}}{V_{out}}$ is the ratio between the in-phase signal V_{in} and the out-of-phase signal V_{out} . [Figure S2a](#) shows the sensitivity analysis based on the two channel heat conduction model. At relatively large spot radius $w = 8.4$ μm above 1 MHz, the five parameters $[k_{z1}, k_{z2}, G_{21}, G_{22}, g]$ dominantly affect the signal $-V_{in}/V_{out}$. These five parameters are extracted simultaneously by fitting the experiments at five modulation frequencies: $f_0 = 1.06$ MHz, 2.16 MHz, 5.10 MHz and 9.80 MHz. To fit the obtained experiment signal $-V_{in}/V_{out}$, we use the nonlinear regression method⁵ to minimize the cost function, which is defined as:

$$W(\mathbf{U}) = \sum_i \sum_j [R_{Exp}(\tau_i, f_{0j}) - F(\tau_i, f_{0j}, \mathbf{U}, \mathbf{P})]^2 \quad (3)$$

where $R_{Exp}(\tau_i, f_{0j})$ is the ratio $-V_{in}/V_{out}$ measured experimentally at the delay time τ_i and the modulation frequency f_{0j} . F is the solution of the two-channel heat conduction model which predicts the signal $-V_{in}/V_{out}$. The vector $\mathbf{U} = [k_{z1}, k_{z2}, G_{21}, G_{22}, g]^T$ is the set of unknown parameters that need to be determined. The vector \mathbf{P} is the vector of control parameters including laser spot radius, thickness, heat capacity and thermal conductivity of the transducer, and heat capacity of the sample. The Simplex algorithm⁵ is used to seek the minimum of the cost function by varying the values of \mathbf{U} iteratively, until the change in \mathbf{U} and W is both smaller than 0.1%.

At the local equilibrium limit, the cross-plane thermal conductivity is simply calculated as the summation of the contribution from each channel:

$$k_z^{eq} = k_{z1} + k_{z2} \quad (4)$$

Supporting Information

The sensitivity for the in-plane thermal conductivity is increased from 0.05 to 0.09 when the laser spot is tightly focused to $w = 4.2 \mu\text{m}$ at low frequency $f = 0.3 \text{ MHz}$, as shown [Figure S2b](#). Therefore, $f_0 = 0.353 \text{ MHz}$ is selected for measuring k_r in the main text. After the cross-plane transport properties $[k_{z1}, k_{z2}, G_{21}, G_{22}, g]$ are determined, the unknown parameter is set to be $\mathbf{U} = [k_{r1}, k_{r2}]^T$ and the cross-plane transport properties are grouped into the vector of control variables \mathbf{P} which are fixed during the nonlinear regression. k_{r1}, k_{r2} are then extracted by minimizing Eq. (3). The in-plane thermal conductivity at the near equilibrium limit is similarly calculated by the summation of the contributions from both channels:

$$k_r^{eq} = k_{r1} + k_{r2} \quad (5)$$

[Table S1](#) reports the best-fit parameters $[k_{r1}, k_{r2}, k_{z1}, k_{z2}, G_{21}, G_{22}, g]$ and the heat capacities of each channel of the TMD alloys. The division of heat capacity into the two channels are described in Section S5.

[Table S1](#). Best-fit parameters $[k_{r1}, k_{r2}, k_{z1}, k_{z2}, G_{21}, G_{22}, g]$ and the heat capacity of the TMD samples $\text{WSe}_{2(1-x)}\text{Te}_{2x}$. Shaded area represents the samples in Td phase while the rest are the samples in the 2H phase.

| x | C_1 | C_2 | k_{r1} | k_{r2} | k_{z1} | k_{z2} | G_{21} | G_{22} | g |
|-----|---------------------|---------------------|----------|----------|----------|----------|---------------------|---------------------|-------------------------------------|
| | MJ/m ³ K | MJ/m ³ K | W/mK | W/mK | W/mK | W/mK | MW/m ² K | MW/m ² K | 10 ¹³ W/m ³ K |
| 0 | 0.693 | 1.287 | 32.1 | 7.2 | 2.05 | 0.4 | 7.15 | 46.3 | 8.0 |
| 0.1 | 0.640 | 1.300 | 10.62 | 3.14 | 0.94 | 0.23 | 1.38 | 34.6 | 4.4 |
| 0.2 | 0.623 | 1.277 | 9.84 | 1.03 | 0.71 | 0.08 | 4.21 | 9.81 | 1.1 |
| 0.4 | 0.613 | 1.227 | 9.72 | 0.34 | 0.65 | 0.06 | 3.99 | 8.97 | 0.65 |
| 0.6 | 0.423 | 1.377 | 3.2 | 0.5 | 0.24 | 0.04 | 26.2 | 34.2 | 0.73 |
| 0.8 | 0.439 | 1.301 | 4.8 | 0.6 | 0.51 | 0.10 | 29.2 | 38.7 | 0.8 |
| 1.0 | 0.443 | 1.237 | 10.41 | 4.64 | 1.14 | 0.21 | 23.2 | 43.1 | 3.3 |

Supporting Information

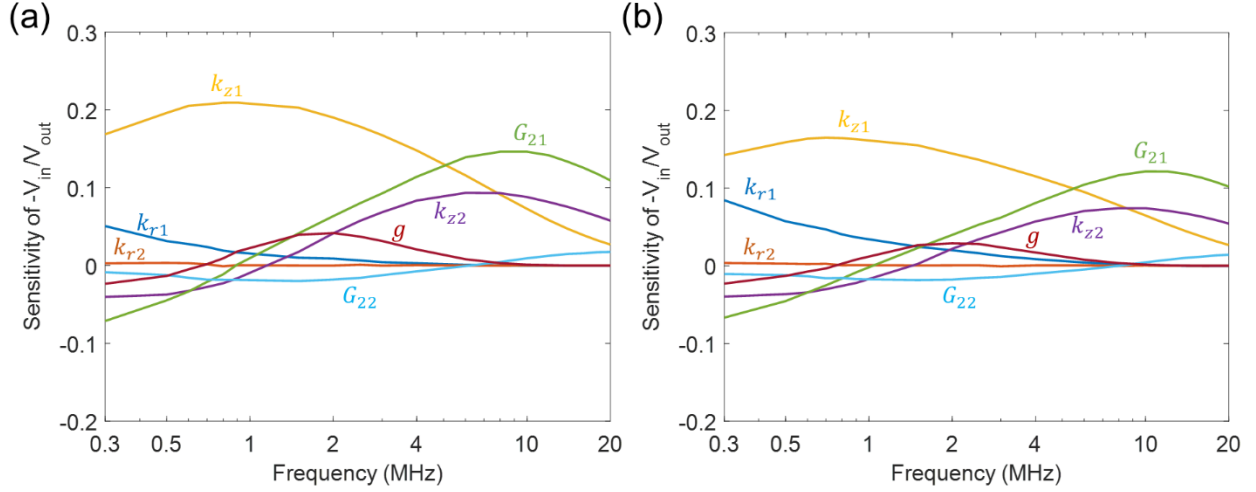


Figure S2. Sensitivity analysis of experimental parameters for a 76 nm Al on $\text{WSe}_{1.2}\text{Te}_{0.8}$ sample as a function of modulation frequency f_0 . (a) Sensitivity of the unknown parameters using a $w = 8.4 \mu\text{m}$ and (b) $w = 4.2 \mu\text{m}$. The parameters for calculating sensitivities are $k_{r1} = 9.7 \text{ W/mK}$, $k_{r2} = 0.3 \text{ W/mK}$, $k_{z1} = 0.65 \text{ W/mK}$, $k_{z2} = 0.05 \text{ W/mK}$, $G_{21} = 4.0 \text{ MW/m}^2\text{K}$, $G_{22} = 8.97 \text{ MW/m}^2\text{K}$ and $g = 6.5 \times 10^{12} \text{ W/m}^3\text{K}$.

S4. Uncertainty analysis.

The uncertainty of the unknown variables \mathbf{U} is estimated using the following propagation formula:^{2,6}

$$\begin{aligned} \text{var}[\mathbf{U}] = & \mathbf{\Sigma}_U^{-1} \left[\sum_j \mathbf{J}_U^T(f_{0j}) \text{var}[\mathbf{R}_{Exp}(f_{0j})] \mathbf{J}_U(f_{0j}) \right] \mathbf{\Sigma}_U^{-1} \\ & + \mathbf{\Sigma}_U^{-1} \mathbf{\Sigma}_{UP} \text{var}[\mathbf{P}] \mathbf{\Sigma}_{UP}^T \mathbf{\Sigma}_U^{-1} \end{aligned} \quad (6)$$

where $\text{var}[\cdot]$ denotes the variance matrix, $\mathbf{J}_U(f_{0j}) = \left(\frac{\partial \mathbf{F}}{\partial \mathbf{U}} \right)_{f_{0j}}$ and $\mathbf{J}_P(f_{0j}) = \left(\frac{\partial \mathbf{F}}{\partial \mathbf{P}} \right)_{f_{0j}}$ are the Jacobi matrices of the vector of model prediction $\mathbf{F} = [F(\tau_1), F(\tau_2), \dots, F(\tau_i), \dots]_{f_{0j}}$ with respect to the unknown parameters \mathbf{U} and the control parameters \mathbf{P} . The $\mathbf{\Sigma}$ matrices are written as:

$$\mathbf{\Sigma}_U = \sum_j \mathbf{J}_U^T(f_{0j}) \mathbf{J}_U(f_{0j}), \quad \mathbf{\Sigma}_{UP} = \sum_j \mathbf{J}_U^T(f_{0j}) \mathbf{J}_P(f_{0j}) \quad (7)$$

Since uncertainties of the control parameters are uncorrelated, the covariance matrix $\text{var}[\mathbf{P}]$ is written as a diagonal matrix:

$$\text{var}[\mathbf{P}] = \text{diag}[\sigma_{k_{Al}}^2, \sigma_{c_{Al}}^2, \sigma_{d_{Al}}^2, \sigma_c^2, \sigma_w^2] \quad (8)$$

where σ is the standard deviation. The uncertainties of the input parameters \mathbf{P} are 10% for the thermal conductivity of Al, 3% for the heat capacity of Al and the substrate, 4% for the Al thickness, and 3% for the laser spot size.

Supporting Information

The term $\Sigma_U^{-1}[\sum_j J_U^T(f_{0j})var[\mathbf{R}_{Exp}(f_{0j})]J_U(f_{0j})]\Sigma_U^{-1}$ describes the uncertainty contributed by the noise of the signal, where the $var[\mathbf{R}_{Exp}(f_{0j})]$ represents the noise of the signal at the frequency f_{0j} , which is obtained by calculating the variance of the signal $-V_{in}/V_{out}$ among five individual measurements at each sampled delay time τ_{0j} . The experimental noise only contributes to less than 5% of the uncertainty, and the majority of the error comes from the uncertainties of the control variables. If \mathbf{U} is a vector of N elements $\mathbf{U} = [u_1, u_2, \dots, u_N]^T$, the covariance matrix $var[\mathbf{U}]$ is a $N \times N$ matrix with the following form:

$$var[\mathbf{U}] = \begin{bmatrix} \sigma_{u_1}^2 & cov[u_1, u_2] & \cdots & cov[u_1, u_N] \\ cov[u_2, u_1] & \sigma_{u_2}^2 & \cdots & cov[u_2, u_N] \\ \vdots & \vdots & \ddots & \vdots \\ cov[u_N, u_1] & cov[u_N, u_2] & \cdots & \sigma_{u_N}^2 \end{bmatrix} \quad (9)$$

where $cov[u_i, u_j]$ is the covariance between u_i and u_j and it is identical to $cov[u_j, u_i]$ so that the $var[\mathbf{U}]$ is a symmetrical matrix. The covariance $cov[u_i, u_j]$ denotes the correlation between the two variables u_i and u_j . If $cov[u_i, u_j]$ is zero, then u_i and u_j are independent. When determining the confidence interval of the multiple parameters, it is also necessary to consider the covariance. The confidence interval for multiple parameters are determined by a quadratic surface in the parameters space:

$$(\mathbf{U} - \mathbf{U}^0)^T (var[\mathbf{U}])^{-1} (\mathbf{U} - \mathbf{U}^0) = \chi_N^2(P = 0.95) \quad (10)$$

where \mathbf{U}^0 denotes the best-fit parameters. $\chi_N^2(P)$ is the N -th order quantile function,⁷ and $P = 0.95$ is the probability of the confidence interval. To estimate the error of k_z^{eq} and k_r^{eq} , we first plot the confidence interval projected to the sub-space of the entire parameter space using the following two equations respectively:

$$([k_{r1}, k_{r2}] - [k_{r1}^0, k_{r2}^0])(var[k_{r1}, k_{r2}])^{-1}([k_{r1}, k_{r2}] - [k_{r1}^0, k_{r2}^0])^T = \chi_2(0.95) \quad (11)$$

and

$$([k_{z1}, k_{z2}] - [k_{z1}^0, k_{z2}^0])(var[k_{z1}, k_{z2}])^{-1}([k_{z1}, k_{z2}] - [k_{z1}^0, k_{z2}^0])^T = \chi_2(0.95). \quad (12)$$

The confidence intervals are generally ellipses as shown in [Figure S3](#). Based on the shape of the confidence interval, the upper and lower limit of k_z^{eq} and k_r^{eq} can be obtained as showed in [Figure S3](#). For example, when determining k_z^{eq} , the line tangential to the ellipse with the equation:

$$k_{z1} + k_{z2} = k_z^{eq} \quad (13)$$

are drawn, and we can determine the uncertainty of k_z^{eq} from the intersect with the two axes.

Supporting Information

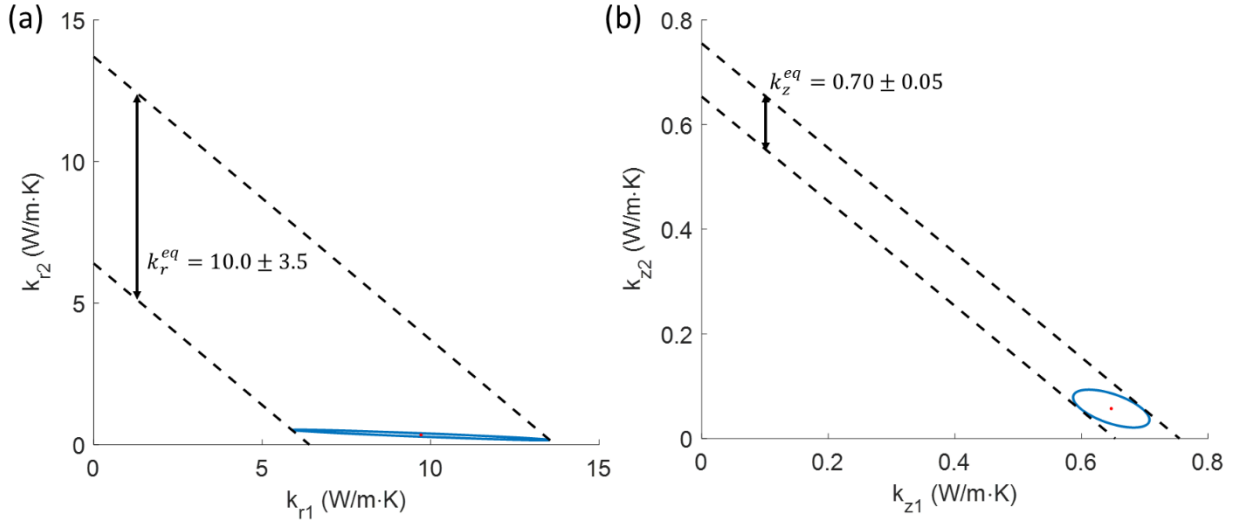


Figure S3. Schematic of the confidence intervals (ellipses with blue solid lines) and the determination of the thermal conductivity at the near equilibrium limit from the confidence interval (dashed black lines). The red dot shows the best fit value. (a) confidence interval of k_{r1} and k_{r2} . (b) confidence interval for k_{z1} and k_{z2} for $\text{WSe}_{1.2}\text{Te}_{0.8}$.

S5. Heat capacity of TMD alloys using the first principles calculations

Virtual crystal approximation for calculating heat capacities. We use the first principles lattice dynamics calculations to determine the heat capacities of TMD alloys. For crystals, the heat capacity could be easily calculated from the phonon dispersions. However, phonon dispersion is not well defined due to the lack of periodicity in the layered TMD alloys with randomly distributed Se and Te atoms on the chalcogen sites. We therefore use the virtual crystal approximation (VCA) to restore the periodicity so that phonon dispersions of alloys can be calculated.⁸ Figure S4 describes the application of VCA to the TMD alloys in 2H phase as an example. A virtual crystal is created by replacing the randomly distributed Se and Te atoms with a virtual atom X, whose atomic mass (m_X), lattice constants (a and c) and harmonic force constants ϕ are a compositional average of 2H WSe_2 and 2H WTe_2 :

$$\begin{aligned}
 m_X &= xm_{\text{Te}} + (1-x)m_{\text{Se}} \\
 a &= xa_{\text{WSe}_2} + (1-x)a_{\text{WTe}_2} \\
 c &= xc_{\text{WSe}_2} + (1-x)c_{\text{WTe}_2} \\
 \phi &= x\phi_{\text{WTe}_2} + (1-x)\phi_{\text{WSe}_2}
 \end{aligned} \tag{14}$$

where x is the fraction of WTe_2 in the alloy $\text{WSe}_{2(1-x)}\text{Te}_{2x}$. Similarly, the VCA is applied to obtain the lattice constants and harmonic force constants of TMD alloys in the Td phase.

Supporting Information

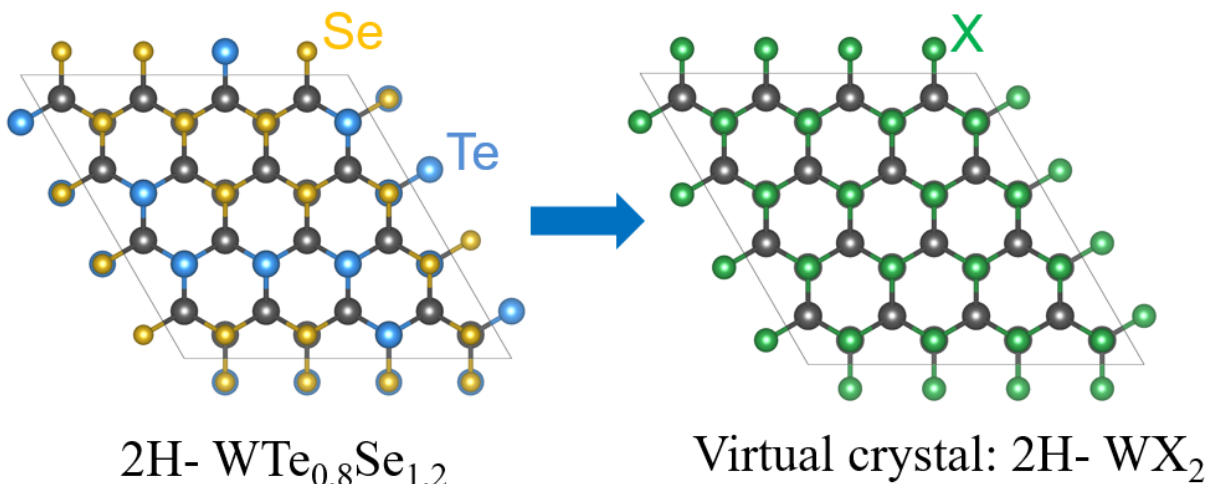


Figure S4. Schematic of virtual crystal approximation for TMD alloys in the 2H phase.

First-principles calculations of the harmonic force constants. First-principles calculations are carried out using Vienna ab-initio Simulation Package (VASP)⁹⁻¹⁰ with the projector augmented wave (PAW) pseudopotential¹⁰ with the local density approximation (LDA). The energy cut-off for the plane-wave basis is set to be 600 eV for all calculations. A $13 \times 7 \times 3$ Monkhorst-Pack mesh (k-mesh) is used to sample the Brillouin zone during the structure optimization. The choice of the energy cutoff and k-mesh ensures that the energy change is smaller than 1 meV/atom when refining these two parameters.¹¹ All materials are relaxed through the conjugate gradient algorithm until the atomic forces are smaller than 5×10^{-6} eV/Å. The obtained lattice parameters after the structural relaxation are shown in Table S2, all agreeing well with the literature values¹²⁻¹³ within 2%.

Table S2. Lattice parameters of WSe₂ and WTe₂ compared with literature values.

| | 2H WSe ₂ | | 2H WTe ₂ | |
|----------|---------------------|-------------------|---------------------|--------------------------|
| | This work | Exp. ^a | This work | Calc. (LDA) ^b |
| <i>a</i> | 3.247 | 3.282 | 3.472 | 3.51 |
| <i>c</i> | 12.792 | 12.961 | 13.804 | 13.90 |
| | Td WSe ₂ | | Td WTe ₂ | |
| | This work | - | This work | Exp. |
| <i>a</i> | 3.248 | - | 3.443 | 3.486 |
| <i>b</i> | 5.852 | - | 6.215 | 6.265 |
| <i>c</i> | 12.679 | - | 13.802 | 14.038 |

a. Ref. ¹²; b. LDA calculation by Ref. ¹³

We use the Phonopy package¹⁴ for extracting the harmonic force constants of TMD alloys. The standard direct method is employed to extract the harmonic and third-order anharmonic force constants.¹⁵ First, we construct a series of supercells containing $3 \times 3 \times 1$ unit cells¹⁶ with different

Supporting Information

atoms perturbed from the equilibrium position by a small displacement $\Delta = 0.03 \text{ \AA}$. Then self-consistent field calculations are performed on each perturbed supercell using VASP, with a $4 \times 4 \times 3$ k-mesh.¹⁶ Interatomic forces are recorded for calculating the force constants using the central differentiation method:

$$\phi_{lb,l'b'}^{\alpha\beta} = -\frac{F_{l'b'}^{\alpha}(u_{lb}^{\alpha} = \Delta) - F_{l'b'}^{\beta}(u_{lb}^{\alpha} = -\Delta)}{2\Delta} \quad (15)$$

where ϕ denotes the harmonic force constants; u denotes the displacement from equilibrium position; α, β, γ are the indices for the directions in Cartesian coordinates; l is the index for a unit cell in the supercell and b is the b -th atom in the unit cell. The phonon dispersions

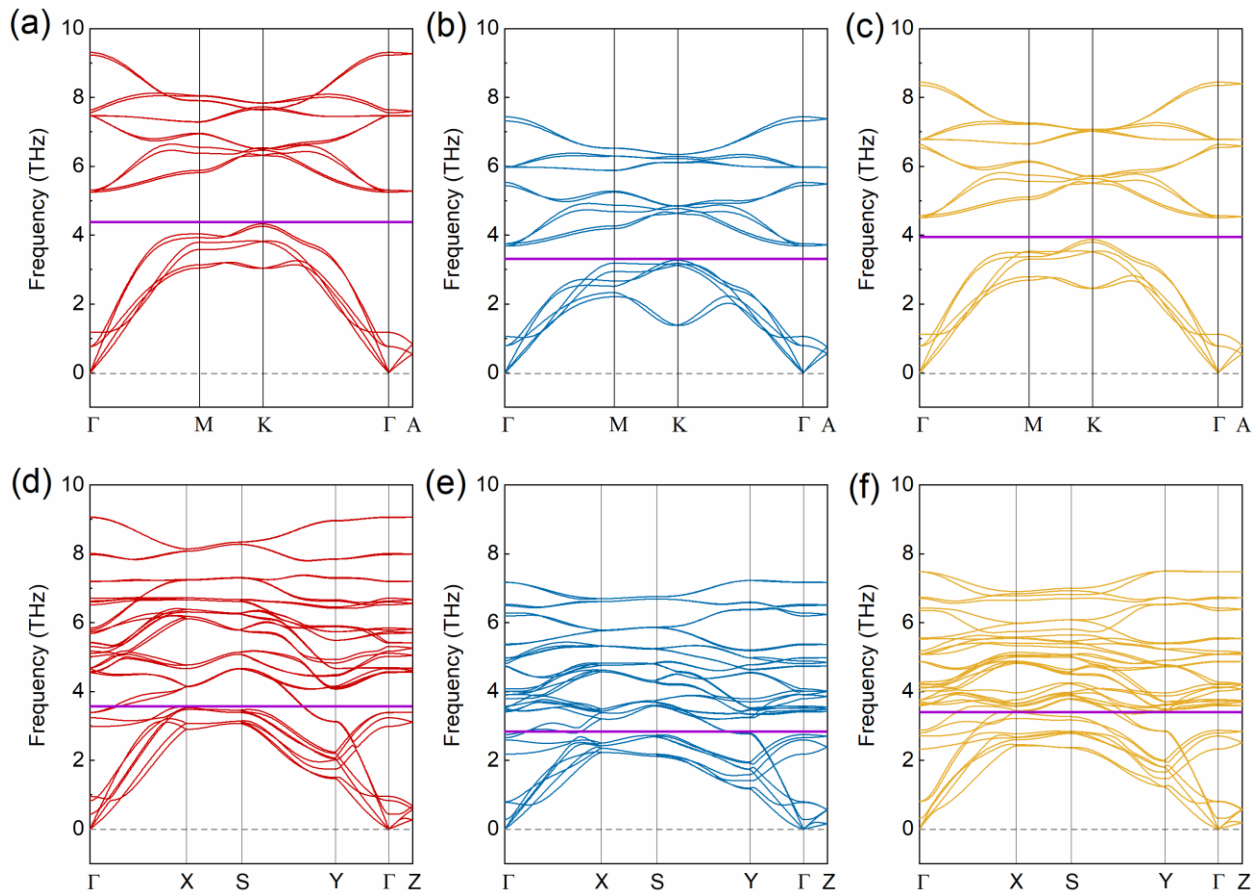


Figure S5. Phonon dispersions of (a) 2H WSe₂, (b) 2H WTe₂ and (c) 2H WSe_{1.2}Te_{0.8}, (d) Td WSe₂, (e) Td WTe₂ and (f) Td WSe_{0.4}Te_{1.6}. The horizontal purple lines show the cutoff frequencies that divide phonons into the low frequency channel and high frequency channels.

Phonon dispersion and heat capacities of TMD alloys. The phonon dispersion is calculated by solving the dynamical equation:

Supporting Information

$$\sum_{b'\beta} D_{bb'}^{\alpha\beta}(\mathbf{q}) e_{b'}^{\beta}(\mathbf{q}s) = [\omega(\mathbf{q}s)]^2 e_b^{\alpha}(\mathbf{q}s) \quad (16)$$

where b and b' are the indices of basis atoms in the unit cell, α and β are the indices of Cartesian coordinates, \mathbf{q} is the phonon wavevector and s is the polarization, ω and e denote the frequency and wave vector, respectively. The dynamic matrix $D_{bb'}^{\alpha\beta}(\mathbf{q})$ is calculated using the harmonic force constants:

$$D_{bb'}^{\alpha\beta}(\mathbf{q}) = \frac{1}{\sqrt{m_b m_{b'}}} \sum_{\mathbf{l}'} \phi_{0b,\mathbf{l}'b'}^{\alpha\beta} \cdot \exp[i\mathbf{q} \cdot (\mathbf{R}(\mathbf{l}'))] \quad (17)$$

where m_b is the mass of the b -th atom in the unit cell and $\mathbf{R}(\mathbf{l}')$ is the lattice vector of \mathbf{l}' -th unit cell. The calculated phonon dispersions of WSe₂, WTe₂ and TMD alloys in 2H phase and Td phase are shown in Figure S5. After solving the phonon dispersion, the heat capacities are calculated as:

$$C_V = \frac{\partial}{\partial T} \sum_{\mathbf{q}s} \hbar\omega(\mathbf{q}s) \left[\frac{1}{2} + \frac{1}{\exp(\hbar\omega(\mathbf{q}s)/k_B T) - 1} \right] \quad (18)$$

where T is the temperature, k_B is Boltzmann constant and \hbar is the reduced Planck constant. The calculated composition dependent heat capacity C is shown Figure S6. The pure WSe₂ and WTe₂ agrees well with literature values.

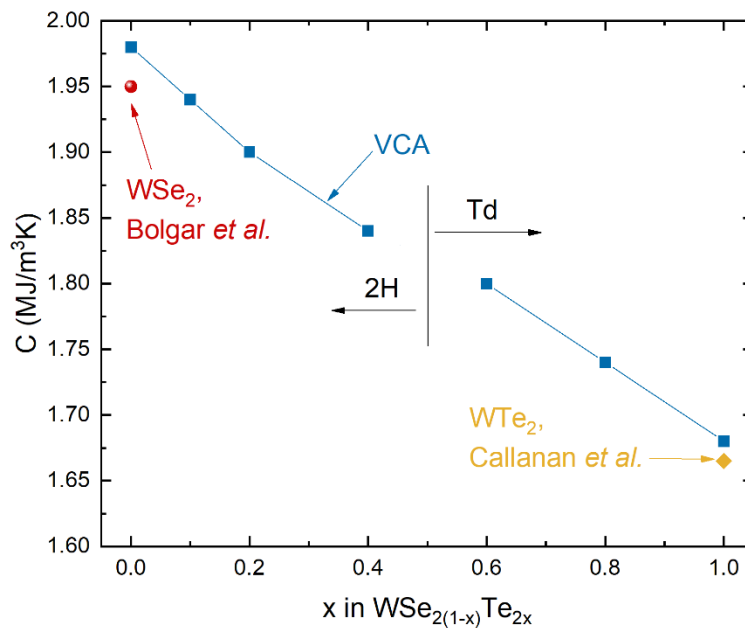


Figure S6. Composition dependent heat capacity of TMD Alloys. The heat capacity of WSe₂ measured Bolgar *et al.*¹⁷ and the heat capacity of WTe₂ measured by Callanan *et al.*¹⁸ are included as references.

S6. Division of the High Frequency and the Low Frequency Channels

Supporting Information

We divide the phonons in the TMD alloys according to the phonon dispersions obtained from VCA. For the alloys 2H phase, the heat capacity is divided into two channels according to the bandgap in the phonon dispersion:

$$C_1 = \frac{\partial}{\partial T} \sum_{\omega_{qs} < \omega_c} \hbar \omega_{qs} n_{qs}(T)$$

$$C_2 = \frac{\partial}{\partial T} \sum_{\omega_{qs} > \omega_c} \hbar \omega_{qs} n_{qs}(T)$$
(19)

where ω_c is the cutoff frequency. Based on the physical picture discussed in Section S2, the cutoff frequency ω_c should be set to include all acoustic phonons with large group velocities. Therefore, we set ω_c to the maximum frequency of LA/LO branches at Brillouin zone boundaries, as shown in Figure S5. After setting the cutoff frequency, the heat capacities can be divided into the two channels, as shown in Figure S7a-b.

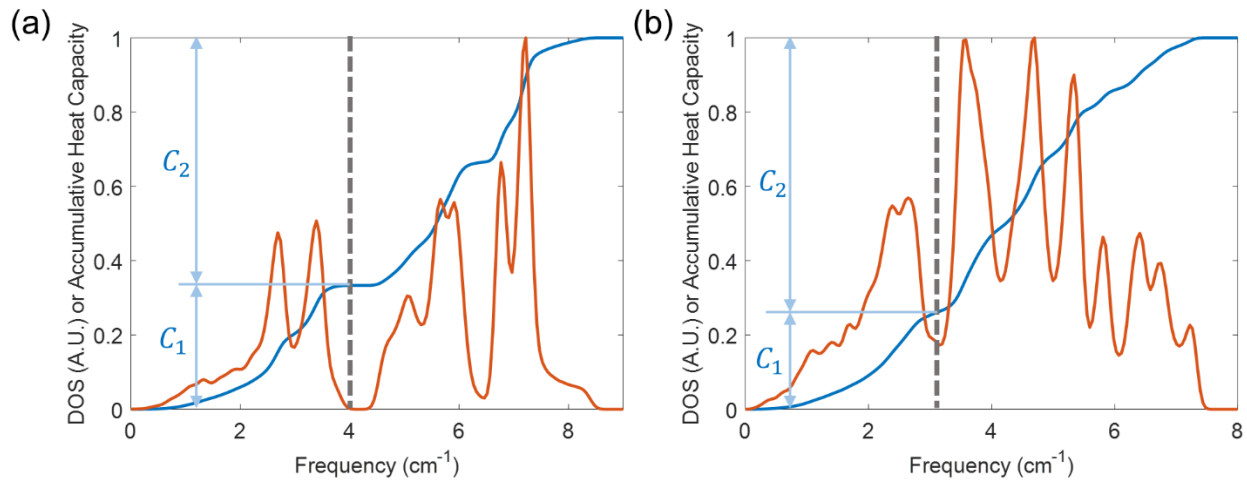


Figure S7. (a) Division of the low-frequency and the high frequency channels according to the phonon bandgap in 2H $\text{WSe}_{1.2}\text{Te}_{0.8}$. (b) Division of the low-frequency and the high frequency channels for Td $\text{WSe}_{0.4}\text{Te}_{1.6}$.

References:

1. Wilson, R. B.; Feser, J. P.; Hohensee, G. T.; Cahill, D. G., Two-Channel Model for Nonequilibrium Thermal Transport in Pump-Probe Experiments. *Phys. Rev. B* **2013**, *88*, 144305.
2. Jiang, P.; Qian, X.; Gu, X.; Yang, R., Probing Anisotropic Thermal Conductivity of Transition Metal Dichalcogenides Mx_2 ($\text{M} = \text{Mo}, \text{W}$ and $\text{X} = \text{S}, \text{Se}$) Using Time-Domain Thermoreflectance. *Adv. Mater.* **2017**, *29*, 1701068.
3. Jain, A.; McGaughey, A. J. H., Thermal Transport by Phonons and Electrons in Aluminum, Silver, and Gold from First Principles. *Phys. Rev. B* **2016**, *93*.
4. Hostetler, J. L.; Smith, A. N.; Czajkowsky, D. M.; Norris, P. M., Measurement of the Electron-Phonon Coupling Factor Dependence on Film Thickness and Grain Size in Au, Cr, and Al. *Applied Optics* **1999**, *28*, 3614.

Supporting Information

5. Maros, I., *Computational Techniques of the Simplex Method*: Boston, 2003.
6. Yang, J.; Ziade, E.; Schmidt, A. J., Uncertainty Analysis of Thermoreflectance Measurements. *Rev. Sci. Instrum.* **2016**, *87*, 014901.
7. Chew, V., Confidence, Prediction and Tolerance Regions for the Multivariate Normal Distribution. *Journal of the American Statistical Association* **1966**, *61*, 605-617.
8. Abeles, B., Lattice Thermal Conductivity of Disordered Semiconductor Alloys at High Temperatures. *Phys. Rev.* **1963**, *131*, 1906-1911.
9. Kresse, G.; Furthmuller, J., Efficiency of Ab-Initial Total Energy Calculations for Metals and Semiconductors Using a Plane-Wave Basis Set. *Comput. Mater. Sci.* **1996**, *6*, 15-50.
10. Kresse, G.; Joubert, D., From Ultrasoft Pseudopotentials to the Projector Augmented-Wave Method. *Phys. Rev. B* **1991**, *59*.
11. Gu, X.; Yang, R., Phonon Transport in Single-Layer Transition Metal Dichalcogenides: A First-Principles Study. *Appl. Phys. Lett.* **2014**, *105*, 131903.
12. Schutte, W. J.; Boer, J. L. d.; Jellinek, F., Crystal Structures of Tungsten Disulfide and Diselenide. *J. Solid State Chem.* **1987**, *70*, 207-209.
13. Kumar, A.; Ahluwalia, P. K., Electronic Structure of Transition Metal Dichalcogenides Monolayers 1h-Mx2 (M = Mo, W; X = S, Se, Te) from Ab-Initio Theory: New Direct Band Gap Semiconductors. *The European Physical Journal B* **2012**, *85*, 186.
14. Togo, A.; Tanaka, I., First Principles Phonon Calculations in Materials Science. *Scripta Mater.* **2015**, *108*, 1-5.
15. Esfarjani, K.; Stokes, H. T., Method to Extract Anharmonic Force Constants from First Principles Calculations. *Phys. Rev. B* **2008**, *77*.
16. Lindroth, D. O.; Erhart, P., Thermal Transport in Van Der Waals Solids from First-Principles Calculations. *Phys. Rev. B* **2016**, *94*, 115205.
17. Bolgar, A. S.; Trofimova, Z. A.; Yanaki, A. A., Methods of Investigation and Properties of Powder Materials. *Powder Metall. Met. Ceram.* **1990**, *29*, 382.
18. Callanan, J. E.; Hope, G. A.; Weir, R. D.; Jr., E. F. W., Thermodynamics Properties of Tungsten Ditelluride I. The Preparation and Low Temperature Heat Capacity at Temperatures from 6 K to 326 K. *J. Chem. Thermodyn.* **1992**, *24*, 627-638.